2024 IEEE/ASME International Conference on Advanced Intelligent Mechatronics (AIM)
July 15-19, 2024. Boston, MA, USA

Structural Compliance Analysis and Experiment of a 4-DoF Parallel Robot

Ming-Yang Cheng, Hao-Chun Liao, and Chao-Chieh Lan, *Senior Member*, *IEEE*

***Abstract*—Pick-and-place automation requires robots to have at least three translational (3T) and one rotational (1R) degrees of freedom. Parallel robots usually include four limbs connected to a traveling plate to generate 3T1R motion. For the four limbs to be arranged with rotational symmetry, complicated types of passive joints and traveling plates are required, which make 3T1R robots structurally weaker and prone to wear and clearance issues. This paper presents a new 3T1R parallel robot that uses only revolute joints as the active and passive joints. Compared with other joint types, revolute joints are structurally simpler and stronger. They have an unlimited range of motion and can be preloaded to eliminate clearance. The proposed robot allows the four limbs to be connected with rotational symmetry. Compliance analysis shows that the 4-DoF robot has a homogenous compliance distribution. Experiments are given to verify that the robot can achieve low structural compliance when compared with existing counterparts. The robot is expected to provide an alternative solution in pick-and-place applications.**

***Index Terms*—Parallel robot, 3T1R motion, H4-type traveling plate, rotational symmetry, structural compliance.**

I. INTRODUCTION

Picking, placing, and palletizing products are tasks that are commonly performed in many manufacturing industries. To accomplish these tasks, industrial robots must have at least three translational degrees of freedom (3T) along three perpendicular axes, to move a product, and one rotational degree of freedom (1R) along the vertical axis, to adjust the orientation of the product. This type of motion is known as the Schönflies motion [1]. SCARA (Selective Compliance Articulated Robot Arm) robots are serial robots that have been used to achieve the Schönflies motion. Parallel robots [1-15] developed to achieve the Schönflies motion are known as the 3T1R parallel robots. Compared with serial robots, a parallel robot consists of multiple parallel limbs that connect the end-effector to the fixed base. Because the limbs are closed and the actuators are fixed to the base, parallel robots intuitively have higher structural rigidity and higher speed than serial robots with open-loop limbs and moving actuators. Due to their high speed and rigidity, parallel robots are preferred in manufacturing and automation industries.

Delta-type parallel robots [16-18] connect the end-effector to the fixed base using three identical limbs. Each limb includes a spatial parallel four-bar mechanism to allow Delta-type robots to generate three translational motions. To further achieve the Schönflies motion, a fourth identical limb can be added between the fixed base and the end-effector [1-7]. Different traveling plate types [1-7] have been used to connect the four limbs to rotate the end-effector. The H4 type [1, 3] allows the simplest traveling plate structure among them. However, the four limbs cannot be placed with rotational symmetry (i.e., actuators at 90° relative to each other) due to singularity issues [19]. Other traveling plate types, such as I4 in [2], Par4 in [4-5], and X4 in [6-7], require a larger number of components or joints and hence are structurally more complicated than the H4 type. By contrast, I4, Par4, and X4 types allow the four limbs to be placed symmetrically. Identical limbs arranged with rotational symmetry have the advantage of generating an axially symmetric workspace and footprint. The overlapping of axially symmetric workspace and footprint makes the robots compact with high workspace-to-footprint ratios. Robots with rotationally symmetric limbs also ensure a homogenous distribution of end-effector force, velocity, and compliance within the workspace. Other non-Delta-type parallel robots have been developed to achieve the Schönflies motion using limbs with [8-10] or without [11-15] rotational symmetry. Although the workspace is not axially symmetric for parallel robots that do not have rotational symmetry, the rotational range [11] or translational range [14] of the end-effector can be increased. The number of limbs can also be reduced [12].

Unlike parallel spherical mechanisms [20-24], which exclusively rely on revolute joints for their passive joint configuration, 3T1R parallel robots can employ spherical [1-6, 11], universal [7-8, 10], prismatic [9], or revolute joints [12-15] to achieve the Schönflies motion at the end-effector. While revolute joints offer continuous rotation, spherical, universal, and prismatic joints exhibit mechanical limitations that limit their range of motion. Moreover, spherical, universal, and prismatic joints are structurally weaker than revolute joints of equivalent dimensions. When prioritizing factors such as a large workspace, high stiffness, and high payload, the optimal choice for constructing 3T1R parallel robots remains the revolute joints.

This paper introduces a new 4-DoF parallel robot with high structural rigidity. The proposed robot incorporates an H4-type traveling plate due to its structural simplicity. Unlike previous 3T1R parallel robots utilizing the H4-type traveling plate [1, 3], which could not arrange the limbs with rotational symmetry, this paper addresses the issue by proposing a new kinematic chain design. This new chain arrangement allows for the symmetric placement of four identical limbs, which are then connected to the H4-type traveling plate. Thus, the parallel robot achieves both a structurally simplified traveling plate and a compact setup featuring a high workspace-to-footprint ratio. The robot also ensures homogenous kinematics and statics through its operation. Notably, the proposed robot employs only revolute joints for both active and passive joints, setting it apart from existing parallel robots that rely on various joint types. This exclusive use of revolute joints results in simpler limb structures, enhanced durability, and increased stiffness, which lead to

Authors are with the Department of Mechanical Engineering, National Cheng Kung University, Tainan, Taiwan (Corresponding author email: cclan@mail.ncku.edu.tw).

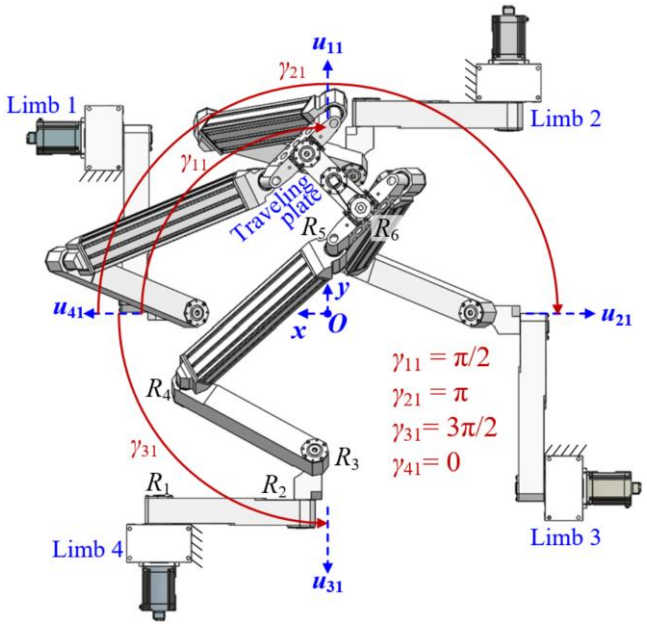

Fig. 1 Bottom-up view of the 4-DoF parallel robot

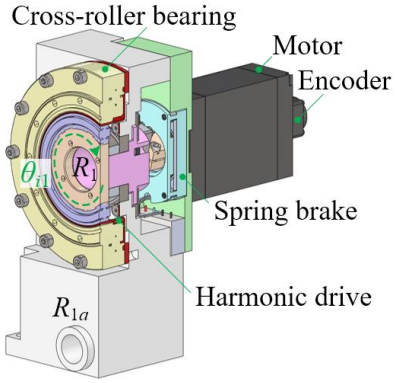

Fig. 2 Cross-sectional view of active revolute joint R_1

high structural rigidity at the end-effector. The robot's link length and overall height can also be minimized compared to Delta-type robots. This reduction in size not only saves space but also mitigates end-effector vibrations during high-speed or high-payload movements. In the following sections, Sec. 2 presents the kinematic structure of the new robot including its limbs and traveling plate. In Sec. 3, the kinematics of the new robot is developed. Sec. 4 investigates the robot workspace and presents a prototype of the 4-DoF robot. Experiments and analyses are conducted in Sec. 5 to verify the low structural compliance of the robot. Finally, Sec. 6 wraps up the paper with concluding remarks.

II. 4-DOF PARALLEL ROBOT STRUCTURE

Illustrated in Fig. 1 is the bottom-up view of the proposed robot. A fixed coordinate ***xyz*** with its origin ***O*** at the robot's center is used as the reference. Four identical limbs are used to connect the traveling plate to the fixed base. Each limb begins with an active revolute joint R_1, originating from the fixed base to actuate a planar parallel four-bar mechanism (Pa). The coupler of the parallel four-bar mechanism connects sequentially to three passive revolute joints R_3, R_4, and R_5. The H-shaped traveling plate includes three rigid members

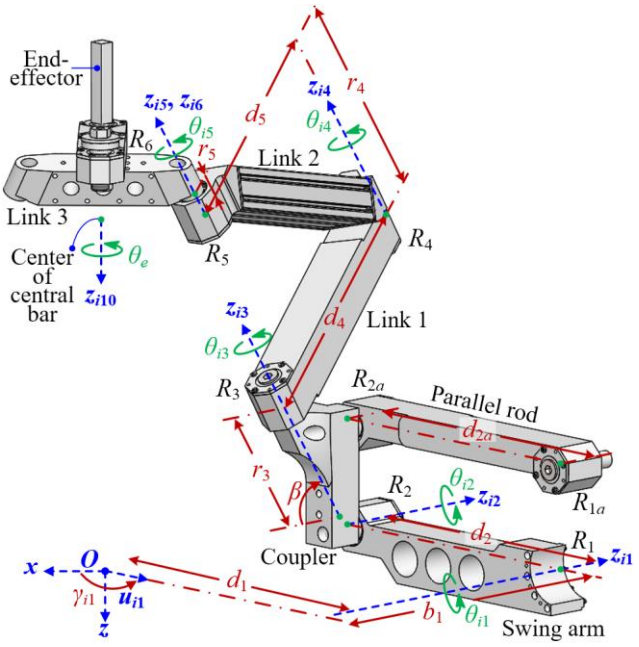

Fig. 3 Configuration of the ith limb

connected by two passive revolute joints R_6. As a result, the parallel robot is characterized as a 2-(2-PaRRR)R kinematic chain that permits the end-effector to have independent translational motions along the ***x***, ***y***, and ***z*** axes and a rotational motion about the $\boldsymbol{\theta}_z$ axis.

In Fig. 1, the active joints' axes are all situated within the ***xy*** plane. Axes $\boldsymbol{u}_{11}$, $\boldsymbol{u}_{21}$, $\boldsymbol{u}_{31}$, and $\boldsymbol{u}_{41}$ serve as reference directions for the respective four limbs. Among these, angles γ_{11}, γ_{21}, and γ_{31} define the orientations of axes $\boldsymbol{u}_{11}$, $\boldsymbol{u}_{21}$, and $\boldsymbol{u}_{31}$ relative to the ***x*** axis, respectively. Axis $\boldsymbol{u}_{41}$ is collinear with the ***x*** axis and hence angle γ_{41} is zero. To ensure rotational symmetry, the values of γ_{11}, γ_{21}, and γ_{31} are designated as $\pi/2$, π, and $3\pi/2$ respectively. As a result, the configuration of the four active joints forms a square, centering around origin ***O***. Fig. 2 shows the cross-sectional view of active joint R_1, which includes an electric motor, a motor encoder, a spring brake, and a harmonic drive for torque amplification. The harmonic drive is supported by a cross-roller bearing to generate the input rotary motion θ_{i1} to the robot.

Fig. 3 shows the configuration of the ith limb. Active joint R_1 is hidden in Fig. 3 for clarity in illustrating the symbols. For each limb, the parallel four-bar mechanism includes a swing arm, a parallel rod, and a coupler, which are connected by active joint R_1 and passive joints R_{1a}, R_2, and R_{2a} that are parallel to R_1. The coupler of the parallel four-bar mechanism is connected to the end-effector through Link 1 and Link 2. Passive joints R_3, R_4, and R_5 are parallel, and they are used to connect Links 1 and 2. Only revolute joints are used for the robot, and only R_1 and R_{1a} are stationary. In Fig. 3, a green point designates the geometric center of each joint. The location of R_1 relative to origin ***O*** is denoted by lengths d_1 and b_1. The swing arm has a length of d_2 and rotates θ_{i1} about axis $\boldsymbol{z}_{i1}$. The inclination angle of axis $\boldsymbol{z}_{i3}$ relative to the ***x*** or ***y*** axis is denoted by β.

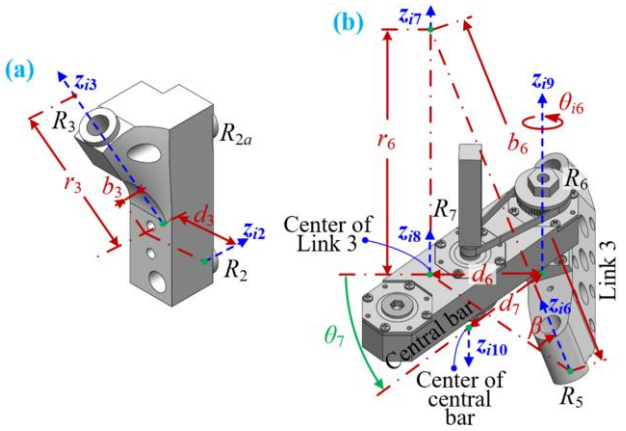

Fig. 4 (a) Configuration of the coupler (b) Configuration of the traveling plate

In Fig. 4(a), lengths d_3, b_3, and r_3 characterize the distances from passive joint R_3 to passive joint R_2 along axes $\boldsymbol{u}_{i1}$, $\boldsymbol{z}_{i2}$, and $\boldsymbol{z}_{i3}$, respectively. Link 1 rotates θ_{i3} about axis $\boldsymbol{z}_{i3}$ and has a length of d_4. Link 2 rotates θ_{i4} about axis $\boldsymbol{z}_{i3}$. The dimensions of Link 2 are characterized by d_5 and r_4, which are lengths perpendicular and parallel to axis $\boldsymbol{z}_{i5}$, respectively.

Fig. 4(b) shows the traveling plate. The link joining the two R_5 joints is denoted as Link 3. For clarity, the other Link 3 is not shown in Fig. 4(b). Passive joint R_6 is parallel to the $\boldsymbol{z}$ axis and placed at the midpoint of Link 3. Length d_6 denotes the distance from R_6 to the center of Link 3. Length d_7 denotes the distance from R_6 to the center of the central bar. Angle θ_7 denotes the rotation of the central bar relative to Link 3. At $\theta_7 = 0°$, we have $d_6 = d_7$. The location of R_5 relative to the central bar's center is denoted by r_6 and b_6. To simplify the geometrical considerations, length r_6 is made equal to $b_6\sin\beta$, thereby ensuring that the central bar's center is at an equivalent elevation as passive joint R_5.

The bottom-up and cross-sectional views of the traveling plate at $\theta_7 = 0°$ are illustrated in Figs. 5(a) and 5(b), respectively. The end-effector is connected to the midpoint of the central bar using a passive joint R_7 with rotation θ_e. Angle θ_{i6} denotes the relative position between R_7 and each R_5 at $\theta_7 = 0°$. To maintain structural symmetry, we have $\theta_{16} = \theta_{26} = \pi/4$ and $\theta_{36} = \theta_{46} = 5\pi/4$, as shown in Fig. 5(a). Hence, the four R_5 joints form a square. A belt drive with a speed ratio of n is used to connect R_6 and R_7. Fig. 5(b) shows the cross-sectional view of the belt drive. When $n > 1$, the belt drive can be used to amplify the rotation of the end-effector. Fig. 5(c) shows the rotations of R_7 and R_6, which is related to n by $n = \theta_e/\theta_7$.

In Figs. 5(a)-5(c), the two Link 3's of the H4-type traveling plate are always parallel regardless of the central bar. Hence, only one link is required to connect the two Link 3's. The four limbs can be evenly connected to the traveling plate with a 90° interval. This differs from existing Delta-type 3T1R parallel robots [2, 4-7] that need to use I4-type, Par4-type, or X4-type traveling plates to ensure rotational symmetry without causing singularities. Using an H4-type traveling plate is advantageous because it requires a minimum number of components and joints to generate the end-effector rotation.

The inspiration for the presented robot stemmed from earlier parallel robots [25-26], which demonstrated the

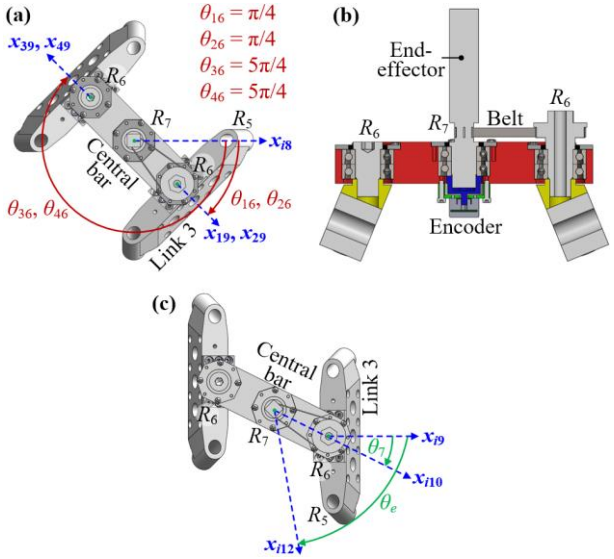

Fig. 5 (a) Bottom-up view of the traveling plate (b) Cross-sectional view of the belt drive (c) Rotation of the central bar and end-effector

feasibility of achieving purely translational motion utilizing three collinear revolute joints in a limb. In [26-27], only revolute joints were used as the passive joints for the three limbs to produce three distinct translational movements.

III. ROBOT KINEMATIC MODELING

Using transformation matrices for derivation, the equation to obtain the swing arm rotations θ_{11}, θ_{21}, θ_{31}, and θ_{41} from the end-effector configuration of x, y, z, and θ_e can be expressed as follows:

$$\begin{bmatrix} S\theta_{11} \\ S\theta_{21} \\ S\theta_{31} \\ S\theta_{41} \end{bmatrix} = \frac{1}{d_2}\begin{bmatrix} -S\gamma_{11}T^{-1}\beta & C\gamma_{11}T^{-1}\beta & -1 \\ -S\gamma_{21}T^{-1}\beta & C\gamma_{21}T^{-1}\beta & -1 \\ -S\gamma_{31}T^{-1}\beta & C\gamma_{31}T^{-1}\beta & -1 \\ -S\gamma_{41}T^{-1}\beta & C\gamma_{41}T^{-1}\beta & -1 \end{bmatrix} \begin{bmatrix} d_7T^{-1}\beta S(\theta_e/n+\theta_{16}-\gamma_{11}) \\ d_7T^{-1}\beta S(\theta_e/n+\theta_{26}-\gamma_{21}) \\ d_7T^{-1}\beta S(\theta_e/n+\theta_{36}-\gamma_{31}) \\ d_7T^{-1}\beta S(\theta_e/n+\theta_{46}-\gamma_{41}) \end{bmatrix} \begin{bmatrix} x \\ y \\ z \\ 1 \end{bmatrix} + \begin{bmatrix} C_1 \\ C_2 \\ C_3 \\ C_4 \end{bmatrix} \quad (1)$$

where

$$C_i = [(b_1+b_3)\cot\beta - (b_6+r_3+r_4+r_5)\csc\beta + r_6 + d_6\cot\beta\sin(\gamma_{i1}-\theta_{i6})]/d_2 \quad i = 1\sim4 \quad (2)$$

In Eq. (1), symbols S, T, and C are used to denote the sine, tangent, and cosine functions, respectively. Angles γ_{i1} and θ_{i6} are constants. When the value of θ_e remains a constant in Eq. (1), the matrix becomes invariant. Hence, the output-to-input position relationship is homogenous within the workspace. When $\theta_{11} = \theta_{21} = \theta_{31} = \theta_{41} = 0°$, the end-effector's configuration is at $x = 0$, $y = 0$, $z = z_0 = -(b_6 + r_3 + r_4 + r_5)\sin\beta + r_6$, and $\theta_e = 0°$, which is denoted as the central position. Taking time derivatives of Eq. (1), the input-output velocity relationship can be obtained as follows:

$$[\dot{\theta}_{11} \quad \dot{\theta}_{21} \quad \dot{\theta}_{31} \quad \dot{\theta}_{41}]^T = \boldsymbol{J}^{-1}[\dot{x} \quad \dot{y} \quad \dot{z} \quad \dot{\theta}_e]^T = \boldsymbol{J}_A\boldsymbol{J}_B[\dot{x} \quad \dot{y} \quad \dot{z} \quad \dot{\theta}_e]^T \quad (3)$$

Table 1 Dimensions of the proposed robot

$\beta = \pi/3$, $d_1 = 298$ mm, $d_2 = 275$ mm, $d_3 = 23$ mm, $d_4 = 260$ mm, $d_5 = 280$ mm, $d_6 = 65$ mm, $d_7 = 65$ mm, $b_1 = 318$ mm, $b_3 = 3.82$ mm, $b_6 = 230$ mm, $r_3 = 149.65$ mm, $r_4 = 240$ mm, $r_5 = 24$ mm, $r_6 = 199.18$ mm, $n = 3$

where

$$\boldsymbol{J}_A = \begin{bmatrix} 1/d_2C\theta_{11} & 0 & 0 & 0 \\ 0 & 1/d_2C\theta_{21} & 0 & 0 \\ 0 & 0 & 1/d_2C\theta_{31} & 0 \\ 0 & 0 & 0 & 1/d_2C\theta_{41} \end{bmatrix}$$

$$\boldsymbol{J}_B = \begin{bmatrix} -S\gamma_{11}T^{-1}\beta & C\gamma_{11}T^{-1}\beta & -1 & d_7T^{-1}\beta C(\theta_e+\theta_{16}-\gamma_{11})/n \\ -S\gamma_{21}T^{-1}\beta & C\gamma_{21}T^{-1}\beta & -1 & d_7T^{-1}\beta C(\theta_e+\theta_{26}-\gamma_{21})/n \\ -S\gamma_{31}T^{-1}\beta & C\gamma_{31}T^{-1}\beta & -1 & d_7T^{-1}\beta C(\theta_e+\theta_{36}-\gamma_{31})/n \\ -S\gamma_{41}T^{-1}\beta & C\gamma_{41}T^{-1}\beta & -1 & d_7T^{-1}\beta C(\theta_e+\theta_{46}-\gamma_{41})/n \end{bmatrix} \quad (4)$$

In Eq. (4), matrix $\boldsymbol{J_B}$ relies solely on dimensional parameters β, d_7, γ_{i1}, and θ_{i6} and is independent of the remaining dimensional parameters. When $\cos\theta_{i1}$ in matrix $\boldsymbol{J_A}$ approaches unity (such as when θ_{i1} ranges from −15° to 15°) and θ_e remains at 0° within matrix $\boldsymbol{J_B}$, the robot closely approaches an invariant $\boldsymbol{J}$. This indicates that the input-output velocity relationship is uniform when the end-effector is around the central position. The input-output velocity relationship is also symmetric about the $z = z_0$ plane.

Using the values of γ_{i1} in Fig. 1 and θ_{i6} in Fig. 5(a), matrix $\boldsymbol{J_B}$ can be reduced as follows:

$$\boldsymbol{J}_B = \begin{bmatrix} -\cot\beta & 0 & -1 & d_7\cot\beta\cos(\theta_e-\pi/4)/n \\ 0 & -\cot\beta & -1 & d_7\cot\beta\cos(\theta_e-3\pi/4)/n \\ \cot\beta & 0 & -1 & d_7\cot\beta\cos(\theta_e-\pi/4)/n \\ 0 & \cot\beta & -1 & d_7\cot\beta\cos(\theta_e+5\pi/4)/n \end{bmatrix} \quad (5)$$

Similarly, Eq. (1) can be reduced as follows using the values of γ_{i1} in Fig. 1 and θ_{i6} in Fig. 5(a):

$$\begin{bmatrix} S\theta_{11} \\ S\theta_{21} \\ S\theta_{31} \\ S\theta_{41} \end{bmatrix} = \frac{1}{d_2}\begin{bmatrix} -T^{-1}\beta & 0 & -1 \\ 0 & -T^{-1}\beta & -1 \\ T^{-1}\beta & 0 & -1 \\ 0 & T^{-1}\beta & -1 \end{bmatrix} \begin{bmatrix} d_7T^{-1}\beta S(\theta_e/n-\pi/4)+C_1 \\ d_7T^{-1}\beta S(\theta_e/n-3\pi/4)+C_2 \\ d_7T^{-1}\beta S(\theta_e/n-\pi/4)+C_3 \\ d_7T^{-1}\beta S(\theta_e/n+5\pi/4)+C_4 \end{bmatrix} \begin{bmatrix} x \\ y \\ z \\ 1 \end{bmatrix} \quad (6)$$

In Eq. (6), the contribution of all four limbs on the end-effector motion along the $\boldsymbol{z}$ axis is the same. The actuation of Limbs 1 and 3 does not affect the end-effector motion along the $\boldsymbol{y}$ axis ($\boldsymbol{u}_{11}$). Similarly, the actuation of Limbs 2 and 4 does not affect the end-effector motion along the $\boldsymbol{x}$ axis ($\boldsymbol{u}_{41}$). The end-effector rotation θ_e requires the simultaneous actuation of all four limbs.

IV. PARALLEL ROBOT WORKSPACE AND PROTOTYPE

4.1 Parallel robot workspace

Fig. 6 shows the workspace and footprint of the parallel robot. The feasible workspace of the parallel robot is confined

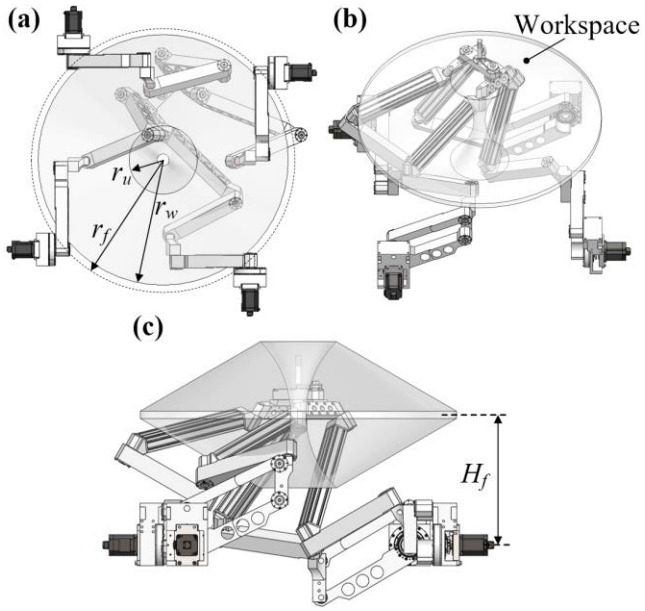

Fig. 6 Workspace and footprint of the parallel robot (a) Top-down view (b) Isometric view (c) Side view

by the outer and inner workspace circles. The largest outer workspace circle occurs at $z = z_0$ and is denoted as r_w. The largest inner workspace circle occurs at $z = z_0 \pm d_2$ and is denoted as r_u. The values of d_4 and d_5 should be increased, and the difference between d_4 and d_5 should be minimized to increase the feasible workspace. Because the four limbs are placed with rotational symmetry, the outer workspace circle is larger than that without rotational symmetry. Similarly, the inner workspace circle is smaller than that without rotational symmetry.

Like the robot's workspace, the robot's footprint is represented by a circle that passes across the four R_2 joints at $z = z_0$. In this context, the footprint radius r_f as shown in Fig. 6(a) is expressed as follows:

$$r_f = (d_1^2 + b_1^2)^{1/2} \quad (7)$$

Hence, the dimension of the robot's footprint depends on the values of d_1 and b_1. Likewise, the robot's height H_f as shown in Fig. 6(c) is defined as the distance between the end-effector center and origin $\boldsymbol{O}$ at $z = z_0$.

$$H_f = -z_0 = (b_6 + r_3 + r_4 + r_5)\sin\beta - r_6 \quad (8)$$

A set of robot dimensions is given in Table 1. These dimensions were chosen such that the outer workspace radius is as close to the radius of the robot footprint as possible. A speed ratio of $n = 3$ was chosen to achieve an end-effector rotation range of ±180°. The radius of the outer workspace circle becomes smaller as z deviates from $z_0 = -358.23$ mm.

4.2 Parallel robot prototype

A prototype of the 4-DoF parallel robot is depicted in Fig. 7. The construction of the prototype was according to the parameters outlined in Table 1. One limb is shown in Fig. 7(a). The active joint includes a motor (Oriental Motor PKP268D42A2) and a harmonic drive (Harmonic Drive SHD-25-50-2SH). The moving links were mainly made of aluminum alloy. The material of the swing arm and Link 2 was partially removed to reduce the total weight. Fig. 7(b) shows the bottom-up view. The total weight of the robot

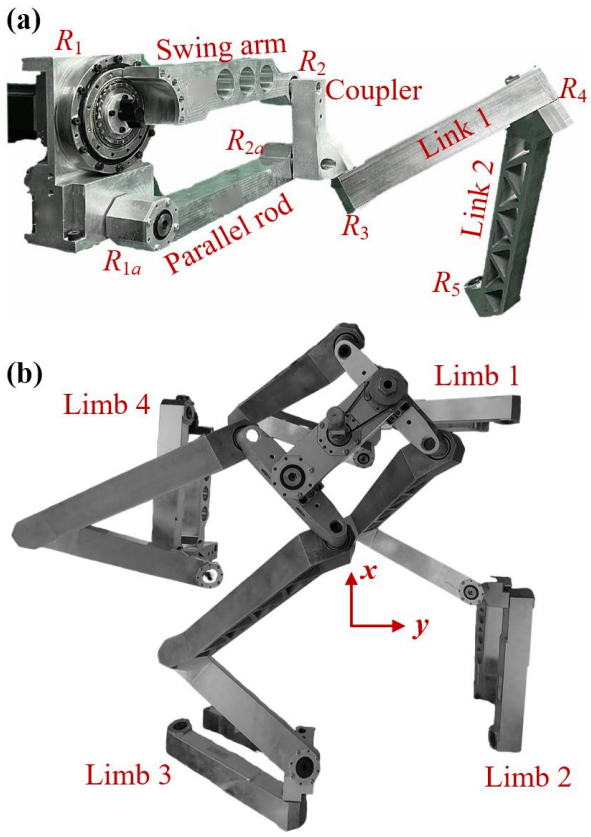

Fig. 7 Robot prototype (a) One limb (b) Bottom-up view

amounts to 43.22 kg, with the moving parts accounting for 28.74 kg. The robot exhibits a payload capacity of 12 kg. The end-effector's speed can reach up to 1.45 m/s and acceleration up to 15.42 m/s^2.

V. STRUCTURAL COMPLIANCE ANALYSIS

5.1 Experimental compliance validation

The compliance of the robot is validated through an experiment on the prototype featured in Fig. 7. For the setup in Fig. 8, the belt drive and passive joint R_7 were temporarily removed to allow ease of measurement. The output link has a square cross section for accurate force and displacement measurements. A linear stage was used to provide a displacement of 1 mm to the output link along different directions. A force sensor was positioned between the output link and the linear stage to obtain the corresponding reaction force. To capture the motion of the output link, a laser displacement sensor was positioned on the opposite side of the output link. In the experiment, the robot was placed at x = 0, y = 225 mm, $z = z_0$, and $\theta_7 = 0°$. The actuation point on the output link was located at $z = z_0 - 146$ mm. The spring brake of each active joint was active to lock the robot. Table 2 presents the experimental results of the robot's compliance. The compliance values along the $\boldsymbol{x}$, $\boldsymbol{y}$, $\boldsymbol{z}$, and $\boldsymbol{\theta}_z$ axes were measured at w_{xx} = 14.63 μm/N, w_{yy} = 14.77 μm/N, w_{zz} = 3.36 μm/N, and $w_{\theta z\theta z}$ = 2.4 rad/kNm respectively. These values align closely with the corresponding simulation outcomes listed in the same table. The simulation results were obtained using ANSYS static structural analysis. The maximum difference between the experimental and simulation results is 12% in the $\boldsymbol{x}$, $\boldsymbol{y}$ and $\boldsymbol{z}$ directions. The robot's compliance along

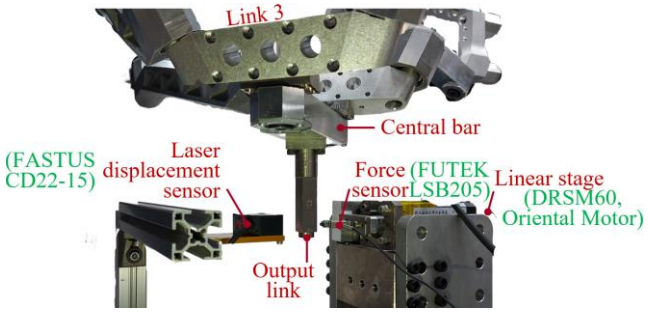

Fig. 8 Configuration for experimental measurement of robot compliance

Table 2 Experimental results of the robot compliance

Compliance	The proposed robot		Robot in [3]
	Simulation	Experiment	Experiment
$\boldsymbol{x}$ axis (w_{xx})	16.40 μm/N	14.63 μm/N	55 μm/N
$\boldsymbol{y}$ axis (w_{yy})	16.26 μm/N	14.77 μm/N	15 μm/N
$\boldsymbol{z}$ axis (w_{zz})	3.50 μm/N	3.36 μm/N	9 μm/N
$\boldsymbol{\theta}_z$ axis ($w_{\theta z\theta z}$)	3.49 rad/kNm	2.40 rad/kNm	N/A

the $\boldsymbol{y}$ axis is very close to the compliance along the $\boldsymbol{x}$ axis. The relatively small compliance value observed along the $\boldsymbol{z}$ axis enables the output link to bear a more substantial payload without incurring significant deformation along the $\boldsymbol{z}$ axis.

5.2 Robot compliance comparison

For comparison, Table 2 includes the compliance values of the parallel robot in [3]. In [3], the 4-DoF robot has a slightly smaller footprint than the proposed robot. However, an H4-type moving platform was used in [3] and hence the four limbs had to be placed asymmetrically to avoid singularities. The four limbs in [3] are separated by 90°, 0°, 90°, and 180°. In the last column in Table 2, the robot's compliance along the $\boldsymbol{x}$ axis greatly exceeds that along the $\boldsymbol{y}$ axis. By contrast, the proposed robot also uses an H4-type moving platform. The symmetrically placed limbs can generate homogeneous compliance along the $\boldsymbol{x}$ and $\boldsymbol{y}$ axes. All compliance values pertaining to the proposed robot are situated below those of [3]. Specifically, along the $\boldsymbol{x}$ and $\boldsymbol{z}$ axes, our robot's compliance values are less than 37% of the corresponding compliance values in [3]. Besides the merit of symmetry, the experiments also validate that using revolute joints as passive joints can make the parallel robot stiffer.

5.3 Compliance distribution in the workspace

Fig. 9 shows the simulation results of robot compliance at different locations in the workspace. On the plane of $z = z_0$, locations $\boldsymbol{A}_1$, $\boldsymbol{B}_1$, $\boldsymbol{C}_1$, and $\boldsymbol{D}_1$ are on a circle with a radius of 225 mm, whereas locations $\boldsymbol{A}_2$, $\boldsymbol{B}_2$, $\boldsymbol{C}_2$, and $\boldsymbol{D}_2$ are on a circle with a radius of 125 mm. Two adjacent locations on the same circle are separated by 90°. The experiment in Sec. 5.1 was conducted at $\boldsymbol{A}_1$. In Fig. 9, the length of each arrow indicates the compliance magnitude and the number beside each arrow indicates the compliance value. The compliance values in the $\boldsymbol{x}$ and $\boldsymbol{y}$ directions are almost identical for all locations. Hence, the uniformity of robot compliance applies to all other locations in the workspace. For all directions, the compliance values are slightly smaller when the moving platform location is closer to the center of the workspace.

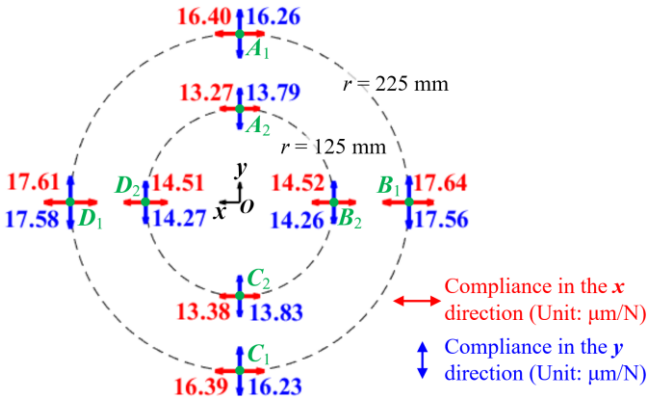

Fig. 9 Compliance distribution in the workspace

VI. CONCLUSIONS

A parallel robot has been introduced to create three linear displacements and one rotation. The new 4-DoF parallel robot uses only revolute joints as the active and passive joints to make the robot stronger and more durable with minimum clearance. The proposed kinematic chain allows four identical limbs to be symmetrically connected to an H4-type traveling plate to generate homogenous force and velocity distributions in the workspace. An actual parallel robot has been built with analysis and experimental validation of the structural compliance at the robot's end-effector. The proposed high-stiffness robot is expected to improve the static and dynamic responses during high-speed or high-payload motion.

REFERENCES

[1] F. Pierrot and O. Company, 1999, "H4: a new family of 4-dof parallel robots," IEEE/ASME International Conference on Advanced Intelligent Mechatronics, 508-513.

[2] S. Krut, M. Benoit, H. Ota, and F. Pierrot, 2003, "I4: A new parallel mechanism for Scara motions," IEEE International Conference on Robotics and Automation, 1875-1880.

[3] C. Corradini, J.-C. Fauroux, and S. Krut, 2003, "Evaluation of a 4-degree of freedom parallel manipulator stiffness," Proceedings of the 11th World Congress in Mechanisms and Machine Science, Tianjin, China.

[4] V. Nabat, M. O. Rodriguez, O. Company, S. Krut, and F. Pierrot, 2005, "Par4: very high speed parallel robot for pick-and-place," IEEE/RSJ International Conference on Intelligent Robots and Systems, 553-558.

[5] F. Pierrot, V. Nabat, O. Company, S. Krut, and P. Poignet, 2009, "Optimal design of a 4-DOF parallel manipulator: From academia to industry," IEEE Transactions on Robotics, 25(2), 213-224.

[6] F. Xie and X.-J. Liu, 2015, "Design and development of a high-speed and high-rotation robot with four identical arms and a single platform," Journal of Mechanisms and Robotics, 7(4), 041015.

[7] O. Altuzarra, B. Şandru, C. Pinto, and V. Petuya, 2011, "A symmetric parallel Schönflies-motion manipulator for pick-and-place operations," Robotica, 29(6), 853-862.

[8] L. Nurahmi, S. Caro, P. Wenger, J. Schadlbauer, and M. Husty, 2016, "Reconfiguration analysis of a 4-RUU parallel manipulator," Mechanism and Machine Theory, 96, 269-289.

[9] S. Yang, T. Sun, and T. Huang, 2017, "Type synthesis of parallel mechanisms having 3T1R motion with variable rotational axis," Mechanism and Machine Theory, 109, 220-230.

[10] M. Gabardi, M. Solazzi, and Antonio Frisoli, 2019, "An optimization procedure based on kinematics analysis for the design parameters of a 4-UPU parallel manipulator," Mechanism and Machine Theory, 133, 211-228.

[11] L.-T. Schreiber and C. Gosselin, 2019, "Schönflies motion PARAllel robot (SPARA): a kinematically redundant parallel robot with unlimited rotation capabilities," IEEE/ASME Transactions on Mechatronics, 24(5), 2273-2281.

[12] B. Belzile, P. K. Eskandary, and J. Angeles, 2019, "Workspace determination and feedback control of a pick-and-place parallel robot: analysis and experiments," IEEE Robotics and Automation Letters, 5(1), 40-47.

[13] C. Tian, Y. Fang, and Q. J. Ge, 2019, "Design and analysis of a partially decoupled generalized parallel mechanism for 3T1R motion," Mechanism and Machine Theory, 140, 211-232.

[14] J. Zhao, C. Wu, G. Yang, C.-Y. Chen, S. Chen, C. Xiong, and C. Zhang, 2022, "Kinematics analysis and workspace optimization for a 4-DOF 3T1R parallel manipulator," Mechanism and Machine Theory, 167, 104484.

[15] H. Simas, R. D. Gregorio, and R. Simoni, 2022, "TetraFLEX: Design and kinematic analysis of a novel self-aligning family of 3T1R parallel manipulators," Journal of Field Robotics, 39(5), 617-630.

[16] R. Jha, D. Chablat, L. Baron, F. Rouillier, and G. Moroz, 2018, "Workspace, joint space and singularities of a family of delta-like robot," Mechanism and Machine Theory, 127, 73-95.

[17] H. Shen, Q. Meng, J. Li, J. Deng, and G. Wu, 2021, "Kinematic sensitivity, parameter identification and calibration of a non-fully symmetric parallel Delta robot," Mechanism and Machine Theory, 161, 104311.

[18] J. Brinker, B. Corves, and Y. Takeda, 2018, "Kinematic performance evaluation of high-speed Delta parallel robots based on motion/force transmission indices," Mechanism and Machine Theory, 125, 111-125.

[19] O. Company and F. Pierrot, 1999, "A new 3T-1R parallel robot," International Conference on Advanced Robotics, 557-562.

[20] H.-C. Hsieh, D.-F. Chen, L. Chien, and C.-C. Lan, 2017, "Design of a parallel actuated exoskeleton for adaptive and safe robotic shoulder rehabilitation," IEEE/ASME Transactions on Mechatronics, 22(5), 2034-2045.

[21] C.-M. Lai, C.-Y. Chu, and C.-C. Lan, 2013, "A two-degrees-of-freedom miniature manipulator actuated by antagonistic shape memory alloys," Smart materials and structures, 22(8), 085006.

[22] C.-Y. Chu, J.-Y. Xu, and C.-C. Lan, 2014, "Design and experiment of a compact wrist mechanism with high torque density," Mechanism and Machine Theory, 78, 65-80.

[23] K.-Y. Wu, Y.-Y. Su, Y.-L. Yu, C.-H. Lin, and C.-C. Lan, 2019, "A 5-degrees-of-freedom lightweight elbow-wrist exoskeleton for forearm fine-motion rehabilitation," IEEE/ASME Transactions on Mechatronics, 24(6), 2684-2695.

[24] Y.-Y. Su, Y.-L. Yu, C.-H. Lin, and C.-C. Lan, 2019, "A compact wrist rehabilitation robot with accurate force/stiffness control and misalignment adaptation," International Journal of Intelligent Robotics and Applications, 3(1), 45-58.

[25] Y.-H. Lai, S.-Y. Huang, and C.-C. Lan, 2022, "A force-controlled parallel robot for large-range stiffness rendering in three dimensions," IEEE Robotics and Automation Letters, 7(2), 1340-1347.

[26] S.-T. Lin, S.-Y. Huang, C.-C. Lan, M. Chidambaram, and V. Sivaramakrishnan, 2023, "Design and experiment of a new translational parallel manipulator with large payload and high repeatability," Mechanism and Machine Theory, 180, 105124.